Superresolution in total internal reflection tomography

Kamal Belkebir, Patrick C. Chaumet, and Anne Sentenac

Institut Fresnel, UMR-CNRS 6133, Campus de Saint Jérôme, case 162, Université d'Aix-Marseille I & III, 13397 Marseille Cedex 20, France

Received October 28, 2004; revised manuscript received March 3, 2005; accepted March 15, 2005

We simulate a total internal reflection tomography experiment in which an unknown object is illuminated by evanescent waves and the scattered field is detected along several directions. We propose a full-vectorial three-dimensional nonlinear inversion scheme to retrieve the map of the permittivity of the object from the scattered far-field data. We study the role of the solid angle of illumination, the incident polarization, and the position of the prism interface on the resolution of the images. We compare our algorithm with a linear inversion scheme based on the renormalized Born approximation and stress the importance of multiple scattering in this particular configuration. We analyze the sensitivity to noise and point out that using incident propagative waves together with evanescent waves improves the robustness of the reconstruction. © 2005 Optical Society of America

OCIS codes: 180.6900, 110.6960, 290.3200.

1. INTRODUCTION

There is considerable interest in developing optical microscopes presenting a lateral resolution below the usual Rayleigh criterion $\lambda/(2\mathrm{NA})$, where λ is the wavelength of the illumination and NA is the numerical aperture of the imaging system, while retaining the convenience of far-field illumination and collection. Among the various ways to ameliorate the resolution, it has been proposed to illuminate the sample with many structured illuminations, namely standing waves, and to mix the different images through simple arithmetic.[1] This technique is very close to optical diffraction tomography, in which the sample is illuminated under various angles of incidence, the phase and intensity of the diffracted far field is detected along several directions of observation,[2–4] and a numerical procedure is used to retrieve the map of the permittivity distribution of the object from the far-field data.[3] Experimental and theoretical studies have shown that using several illuminations permits one to exceed the classical diffraction limit by a factor of 2.[1,3]

Recently, the diffraction tomography approach has been applied to total internal reflection microscopy.[5,6] In total internal reflection tomography (TIRT), the sample is illuminated with different evanescent waves through a prism in total internal reflection. The use of incident evanescent waves permits circumvention of the diffraction limit, as in near-field microscopy, without the inconvenience of bringing a probe close to the sample.[7] A resolution of $\lambda/7$ has been observed in standing-wave total internal reflection fluorescent microscopy.[8] Note that superresolution in the TIRT is obtained only if the objects under test are close to the surface of the prism or even deposited on it.[9]

In all microscopy techniques using several successive illuminations, one needs a numerical procedure to combine the different images and extract the map of the relative permittivity distribution of the object from the scattered far field. In general, one assumes that the object is a weak scatterer so that there is a linear relationship between the scattered field and the relative permittivity of the object, that is, one assumes that the Born approximation is valid.[5,10] In this case, the transverse resolution limit can be inferred from simple considerations on the portion of the Ewald sphere that is covered by the experiment.[3] It is limited by $\lambda/2(n_i+n_d)$ for configurations in which the incident waves propagate in a medium of refractive index n_i while the diffracted waves propagate in a medium of refractive index n_d.[3]

However, the Born approximation restricts the field of application of these imaging techniques to weakly scattering objects whose dielectric contrast with the surrounding medium does not exceed 0.1, typically immersed biological samples. In particular, it cannot be used for imaging manufactured nanostructures or integrated circuits, where the dielectric contrast can reach several unities. Developing reconstruction procedures that account for multiple scattering, in the framework of TIRT, is thus mandatory for a wide domain of applications. It is all the more interesting in that it has been shown recently, in a classical optical tomography configuration, that the presence of multiple scattering permits one to improve the resolution limit beyond that classically foreseen with the study of the Ewald sphere.[11,12]

In this paper, we simulate accurately a TIRT experiment, and we stress the role of the interface and of the multiple scattering. We propose a full-vectorial nonlinear inversion method, and we investigate its power of resolution with respect to the nature—propagative, evanescent, *s*-polarized (TE polarization), *p*-polarized (TM polarization)—of the illuminations. We compare our reconstruction procedure with a linear inversion technique based on the renormalized Born approximation. Last, we

1084-7529/05/091889-9/$15.00

show that the robustness of the reconstruction with respect to noise can be significantly increased by using both propagative and evanescent wave illumination beams.

2. FORMULATION OF THE FORWARD SCATTERING PROBLEM

The coupled dipole method (CDM) was introduced by Purcell and Pennypacker in 1973 to study the scattering of light by nonspherical dielectric grains in free space.[13] In the configuration presented in this article, the objects are deposited on a flat dielectric substrate, but the principle stays the same. The objects under study are represented by a cubic array of N polarizable subunits, and the local field at each subunit of discretization is expressed with the following self-consistent equation:

$$\mathbf{E}(\mathbf{r}_i) = \mathbf{E}^{\mathrm{inc}}(\mathbf{r}_i) + \sum_{j=1, j\neq i}^{N} \overleftrightarrow{\mathbf{T}}(\mathbf{r}_i, \mathbf{r}_j)\alpha(\mathbf{r}_j)\mathbf{E}(\mathbf{r}_j) + \sum_{j=1}^{N} \overleftrightarrow{\mathbf{S}}(\mathbf{r}_i, \mathbf{r}_j)\alpha(\mathbf{r}_j)\mathbf{E}(\mathbf{r}_j), \quad (1)$$

where $\mathbf{E}^{\mathrm{inc}}(\mathbf{r}_i)$ denotes the incident field at the position $\mathbf{r}_i$. The quantity $\alpha(\mathbf{r}_j)$ represents the polarizability of the subunit j. According to the Clausius–Mossotti expression, the polarizability distribution α can be written as

$$\alpha(\mathbf{r}_j) = \frac{3d^3}{4\pi}\frac{\varepsilon(\mathbf{r}_j) - 1}{\varepsilon(\mathbf{r}_j) + 2}, \quad (2)$$

where d is the spacing of the lattice discretization and $\varepsilon(\mathbf{r}_j)$ is the relative permittivity of the object. In Eq. (2), the radiative reaction term is not taken into account in the expression of the polarizability,[14] the weak form of the CDM being accurate enough for the present study.[15] $\overleftrightarrow{\mathbf{T}}$ is the field linear response to a dipole in free space, also called the free-space field susceptibility (see Appendix A). $\overleftrightarrow{\mathbf{S}}$ is the field linear response to a dipole in the presence of a substrate, also called the surface field susceptibility.[16] The elements of this tensor are reported in Appendix B. Once the linear system represented by Eq. (1) is solved, the scattered field in the far-field zone, $\mathbf{E}^{\mathrm{d}}(\mathbf{r})$, can be computed at an arbitrary position $\mathbf{r}$ with

$$\mathbf{E}^{\mathrm{d}}(\mathbf{r}) = \sum_{j=1}^{N} [\overleftrightarrow{\mathbf{T}}^{\mathrm{d}}(\mathbf{r}, \mathbf{r}_j) + \overleftrightarrow{\mathbf{S}}^{\mathrm{d}}(\mathbf{r}, \mathbf{r}_j)]\alpha(\mathbf{r}_j)\mathbf{E}(\mathbf{r}_j). \quad (3)$$

$\overleftrightarrow{\mathbf{T}}^{\mathrm{d}}$ is the field linear response of a dipole in the far field, and hence it corresponds to the term that decays as $1/|\mathbf{r} - \mathbf{r}_j|$ in the expression of $\overleftrightarrow{\mathbf{T}}$. The surface field susceptibility $\overleftrightarrow{\mathbf{S}}^{\mathrm{d}}$ is the field linear response to a dipole in the presence of a substrate when the observation is in the far field zone. In that case, the tensor can be written in a simple analytical form that can be computed rapidly. The expression of $\overleftrightarrow{\mathbf{S}}^{\mathrm{d}}$ is given in Appendix C.

The self-consistent equation (1) can be rewritten in a more condensed form as

$$\mathbf{E} = \mathbf{E}^{\mathrm{inc}} + \bar{\bar{\mathbf{A}}}\mathbf{p}, \quad (4)$$

where $\bar{\bar{\mathbf{A}}}$ is a square matrix of size $3N \times 3N$ and contains all the tensors $\overleftrightarrow{\mathbf{G}}(\mathbf{r}_i, \mathbf{r}_j) = \overleftrightarrow{\mathbf{S}}(\mathbf{r}_i, \mathbf{r}_j) + \overleftrightarrow{\mathbf{T}}(\mathbf{r}_i, \mathbf{r}_j)$. We have

$$\mathbf{E} = [E_x(\mathbf{r}_1), E_y(\mathbf{r}_1), E_z(\mathbf{r}_1), \ldots, E_z(\mathbf{r}_N)],$$

$$\mathbf{E}^{\mathrm{inc}} = [E_x^{\mathrm{inc}}(\mathbf{r}_1), E_y^{\mathrm{inc}}(\mathbf{r}_1), E_z^{\mathrm{inc}}(\mathbf{r}_1), \ldots, E_z^{\mathrm{inc}}(\mathbf{r}_N)],$$

$$\mathbf{p} = [p_x(\mathbf{r}_1), p_y(\mathbf{r}_1), p_z(\mathbf{r}_1), \ldots, p_z(\mathbf{r}_N)],$$

where $\mathbf{E}$ and $\mathbf{E}^{\mathrm{inc}}$ denote the local field and the incident field, respectively. The dipole moment $\mathbf{p}$ is related to the local electric field through $\mathbf{p}(\mathbf{r}_i) = \alpha(\mathbf{r}_i)\mathbf{E}(\mathbf{r}_i)$. Calculating rigorously the local field (4) is time-consuming, especially for a large number of subunits. Hence it is advantageous to first check the validity of the renormalized Born approximation

$$\mathbf{E} \approx \mathbf{E}^{\mathrm{inc}}. \quad (5)$$

In a TIRT experiment, the scattered field is collected at M observation points for L successive illuminations. Let $\mathbf{E}_l^{\mathrm{d}}$ be the scattered field corresponding to the lth illumination; then we can rewrite the far-field equation (3) in the following condensed form:

$$\mathbf{E}_l^{\mathrm{d}} = \bar{\bar{\mathbf{B}}}\mathbf{p}_l, \quad (6)$$

where $l = 1, \ldots, L$ and $\bar{\bar{\mathbf{B}}}$ is a matrix of size $3M \times 3N$. The matrix $\bar{\bar{\mathbf{B}}}$ contains the tensors $\overleftrightarrow{\mathbf{G}}^{\mathrm{d}}(\mathbf{r}_k, \mathbf{r}_j) = \overleftrightarrow{\mathbf{T}}^{\mathrm{d}}(\mathbf{r}_k, \mathbf{r}_j) + \overleftrightarrow{\mathbf{S}}^{\mathrm{d}}(\mathbf{r}_k, \mathbf{r}_j)$, where $\mathbf{r}_j$, $j = 1, \ldots, N$, denotes a point in the discretized object and $\mathbf{r}_k$, $k = 1, \ldots, M$, is an observation point. Note that $\bar{\bar{\mathbf{B}}}$ does not depend on the angle of incidence.

3. FORMULATION OF THE INVERSE SCATTERING PROBLEM

Most reconstruction procedures proposed in the framework of three-dimensional optical tomography have been developed under the Rytov or the Born approximation. In this case, the amplitude of the plane wave with wave vector $\mathbf{k}_{\mathrm{d}}$, diffracted by an object illuminated by a plane wave with wave vector $\mathbf{k}_{\mathrm{inc}}$, is proportional to the Fourier transform of the dielectric contrast $\varepsilon(\mathbf{r}) - 1$ taken at $\mathbf{k}_{\mathrm{d}} - \mathbf{k}_{\mathrm{inc}}$. Thus, if the Fourier space is accurately described by taking a sufficient number of incident and observation angles, it is possible to obtain the map of permittivity of the object by performing a three-dimensional inverse Fourier transform of the diffracted field.[3,10] However, in general, the set of measurements and illuminations is discrete and limited, and there are missing cones in the Fourier space representation. When the Born approximation is assumed, Eq. (6) is linear with respect to the polarizability distribution α. In this case, the incomplete linear system linking the permittivity to the measured far field can be solved in the least-mean-squares sense by using backpropagation algorithms,[4] conjugate gradient techniques,[17] or singular value decomposition.[5,9,18] Note that these techniques require the assumption that the unknown object is entirely confined in a bounded box (test

domain or domain of investigation). This *a priori* information can be used to increase the resolution of the inversion.

To avoid the Born approximation, several nonlinear reconstruction procedures such as the conjugate gradient, modified gradient, and hybrid methods[19–21] have been developed, especially in the microwave domain. In these iterative methods, the field in the scattering domain Ω is no longer assumed to be the incident field. The modified gradient method consists in updating simultaneously the contrast of permittivity as well as the total field inside the investigating domain Ω by minimizing a cost functional involving the residual errors of both Eqs. (4) and (6). In the conjugate gradient method, the total field inside Ω is considered at each iteration step as a fixed solution of Eq. (4) for the best available estimation of the contrast permittivity, and the contrast permittivity is determined by minimizing a cost functional involving the sole residual error of Eq. (6). The hybrid method combines ideas of the two approaches mentioned above. Due to their computational cost, very few have been extended to the vectorial three-dimensional case. Recently, it has been proposed to reconstruct the induced dipoles, $\mathbf{p}(\mathbf{r})=\alpha(\mathbf{r})\mathbf{E}(\mathbf{r})$ in the test domain, by minimizing a cost functional involving the linear far-field equation (6), then calculating the field inside the box with Eq. (4), and deducing the permittivity through the polarizability. With adequate postprocessing, this technique led to satisfactory results for objects with a moderate dielectric constant.[22] In a more advanced method, namely the contrast source inversion method,[23,24] the induced dipoles are reconstructed iteratively by minimizing at each iteration step a cost functional involving both the far-field equation (6) and the near-field equation (4). In the present algorithm, the polarizability in the test domain, $\alpha(\mathbf{r})$, is modified so as to minimize a cost functional involving Eq. (6). At each step of the iterative procedure, the local field is obtained by solving Eq. (4) for the available estimation of the polarizability. In the present section, we briefly present this nonlinear reconstruction procedure, extended to the stratified case.

The geometry of the problem is depicted in Fig. 1. The object under test is assumed to be confined in an investigating domain $\Omega\subset\mathbb{R}^3$ and illuminated successively by $l=1,\ldots,L$ electromagnetic excitations $\mathbf{E}^{\text{inc}}_{l=1,\ldots,L}$. For each excitation l, the scattered field $\mathbf{f}_l$ is measured on a surface Γ at M points and located outside the investigating domain Ω. The inverse scattering problem is stated as finding the permittivity distribution ε inside the investigating area Ω such that the associated scattered field matches the measured field $\mathbf{f}_{l=1,\ldots,L}$.

The sequence $\{\alpha_n\}$ is built up according to the following recursive relation:

$$\alpha_n=\alpha_{n-1}+a_n d_n, \tag{7}$$

where the updated polarizability α_n is deduced from the previous one, α_{n-1}, by adding a correction $a_n d_n$. This correction is composed of two terms: a scalar weight a_n and an updating direction d_n. Once the updating direction d_n is found (this step will be specified later in the paper), the scalar weight a_n is determined by minimizing the cost functional $\mathcal{F}_n(\alpha_n)$ involving the residual error $\mathbf{h}_{l,n}$ on the scattered field computed from observation equation (6):

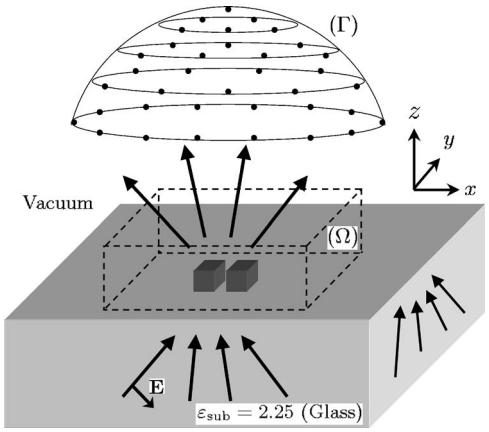

Fig. 1. Illumination and detection configuration of the TIRT experiment. The observation points are regularly placed on the half-sphere Γ (with a radius of 400λ). The illumination is as represented by the arrows, corresponding to a plane wave propagating toward the positive values of z. For the TIRT experiments, the authors took as illumination 16 plane waves in both the planes (x,z) and (y,z), either in p or s polarization. The angle between the incident wave vector and the z axis ranges over −80 to 80 deg.

$$\mathbf{h}_{l,n}=\mathbf{f}_l-\bar{\bar{\mathbf{B}}}\alpha_n\mathbf{E}_{l,n}, \tag{8}$$

with $\mathbf{E}_{l,n}$ being the total electric field that would be present in Ω if the polarizability distribution were α_{n-1}, i.e., solution of the forward problem with α_{n-1}. This field can be written symbolically from Eq. (4) as

$$\mathbf{E}_{n,l}=[\bar{\bar{\mathbf{I}}}-\bar{\bar{\mathbf{A}}}\alpha_{n-1}]^{-1}\mathbf{E}^{\text{inc}}_l, \tag{9}$$

with $\bar{\bar{\mathbf{I}}}$ being the identity matrix.

The cost functional $\mathcal{F}_n(\alpha_n)$ mentioned above that is minimized at each iteration step reads as

$$\mathcal{F}_n(\alpha_n)=\frac{\sum_{l=1}^{L}\|\mathbf{h}_{l,n}\|_\Gamma^2}{\sum_{l=1}^{L}\|\mathbf{f}_l\|_\Gamma^2}=W_\Gamma\sum_{l=1}^{L}\|\mathbf{h}_{l,n}\|_\Gamma^2, \tag{10}$$

where the subscript Γ is included in the norm $\|\cdot\|$ and later the inner product $\langle\cdot|\cdot\rangle$ in L^2 to indicate the domain of integration.

Note that substituting the expression of the polarizability α_n derived from Eq. (7) into Eq. (10) leads to a polynomial expression with respect to the scalar coefficient a_n. Thus the minimization of the cost functional $\mathcal{F}_n(\alpha_n)$ is reduced to the minimization of a simple cost function $\mathcal{F}_n(\alpha_n)$. Moreover, for the particular case of a dielectric material, i.e., the polarizability α is real, the cost function $\mathcal{F}_n(a_n)$ takes the following form:

$$\mathcal{F}_n(a_n)=W_\Gamma\sum_{l=1}^{L}(\|\mathbf{h}_{l,n-1}\|_\Gamma^2+a_n^2\|\bar{\bar{\mathbf{B}}}d_n\mathbf{E}_{l,n}\|_\Gamma^2 - 2a_n\,\text{Re}\langle\mathbf{h}_{l,n-1}|\bar{\bar{\mathbf{B}}}d_n\mathbf{E}_{l,n}\rangle_\Gamma). \tag{11}$$

In this case, the unique minimum of $\mathcal{F}_n(a_n)$ is reached for

$$a_n = \frac{\sum_{l=1}^{L} \mathrm{Re}\langle \mathbf{h}_{l,n-1} | \bar{\bar{\mathbf{B}}} d_n \mathbf{E}_{l,n} \rangle_\Gamma}{\sum_{l=1}^{L} \| \bar{\bar{\mathbf{B}}} d_n \mathbf{E}_{l,n} \|_\Gamma^2}. \tag{12}$$

As updating direction d_n, the authors take the Polak–Ribière conjugate gradient direction

$$d_n = g_{n;\alpha} + \gamma_n d_{n-1}, \tag{13}$$

where g_n is the gradient of the cost functional $\mathcal{F}_n$ with respect to the polarizability assuming that the total fields $\mathbf{E}_l$ do not change.

$$g_{n;\alpha} = -W_\Gamma \sum_{l=1}^{L} \mathbf{E}_{l,n}^* \cdot \bar{\bar{\mathbf{B}}}^\dagger \mathbf{h}_{l,n-1}, \tag{14}$$

in which $\mathbf{u}^*$ denotes the complex conjugate of $\mathbf{u}$ and $\bar{\bar{\mathbf{B}}}^\dagger$ represents the transpose complex conjugate matrix of the matrix $\bar{\bar{\mathbf{B}}}$.

The scalar coefficient γ_n is defined as in the Polak–Ribière conjugate gradient method[25]:

$$\gamma_n = \frac{\langle g_{n;\alpha} | g_{n;\alpha} - g_{n-1;\alpha} \rangle_\Gamma}{\| g_{n-1;\alpha} \|_\Gamma^2}. \tag{15}$$

To complete the inverse scheme, we need to specify the initial guess. As initial estimate for α_0, the authors take the estimate obtained by the backpropagation procedure. This technique is described in detail for the two-dimensional problem in Refs. 26–28. The extension to the three-dimensional problem is described in Appendix D.

4. NUMERICAL EXPERIMENTS

We check the performance of the inverse procedure on synthetic data by simulating a TIRT experiment with the CDM. We consider two cubes of side $a=\lambda/4$, of relative permittivity 2.25, separated by a distance $c=\lambda/10$, deposited on a semi-infinite medium of relative permittivity $\varepsilon_s=2.25$ (as depicted in Fig. 1). The superstrate is vacuum, while the substrate is made of glass. The object is illuminated by 16 plane waves coming from the substrate: eight plane waves in the (x,z) plane and eight plane waves in the (y,z) plane. The plane waves can be p or s polarized. Let θ_l^{inc} be the angle of incidence with respect to the z axis corresponding to the lth illumination. The amplitude and phase of the scattered fields are detected at $M=65$ points regularly distributed on a half-sphere Γ (see Fig. 1). The radius of the sphere is 400λ, so that only far-field component data are considered. The azimuthal angle of observation, θ, defined as the angle between the diffracted wave vector and the z axis, ranges from -80 to 80 deg. In all examples, the synthetic data are computed with a mesh size of $d=\lambda/40$, which differs from the one used in the inversion, $d=\lambda/20$. In all reported results, the investigation domain is a box of size $1.25\lambda \times 0.75\lambda \times 0.6\lambda$ surrounding the cubes, except in Fig. 5, where the size of the box is $1.25\lambda \times 0.75\lambda \times 1.2\lambda$. We display the map of the reconstructed relative permittivity distribution after enough iterations for the cost function to reach a plateau. During the minimization process, the value of the relative permittivity was enforced not to exceed 2.25; thus the convergence was obtained within 100 iterations.

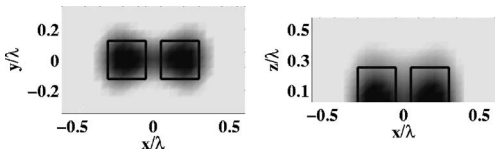

Fig. 2. Left side: map of the relative permittivity in the plane (x,y) just above the substrate, i.e., $z=\lambda/40$. Right side: map of the relative permittivity in the plane (x,z) for $y=0$. We have $a=\lambda/4$, $c=\lambda/10$, $\varepsilon_s=2.25$, $\theta^{\mathrm{inc}} \in [-80,80]$ deg, and p-polarized incident waves.

In Fig. 2, we plot the map of relative permittivity obtained with the nonlinear inversion procedure scheme. The left side corresponds to the map of the relative permittivity in the plane (x,y) just above the substrate, i.e., at $z=\lambda/40$, and the right side corresponds to the map of the relative permittivity in the plane (x,z) for $y=0$. The incident field is p polarized, and the objects are illuminated with both propagative and evanescent waves: $\theta^{\mathrm{inc}} \in [-80,-80]$ deg. Note that, except for Fig. 6, we consider only p-polarized illuminations. One can see that the two objects are perfectly resolved and that the permittivity level saturates at 2.25 inside the cubes. The map of permittivity displayed in Fig. 2, obtained with the nonlinear algorithm, without any noise on the synthetic data and in a "complete" configuration, with evanescent and propagative illuminations, can be considered a reference for all the following reconstructions.

A. Influence of the Substrate

In many numerical simulations of TIRT,[5,9] the object is assumed to be immersed in a homogeneous medium and illuminated by evanescent waves. Yet, the generation of an evanescent wave necessitates the presence of an interface close to the object. Hence this approach amounts to neglecting the influence of the interface on the field scattered by the object. The main advantage of this assumption is that, the free-space susceptibility tensor being a convolution operator with a simple analytical formulation in the direct space, the calculations are greatly simplified in the inversion procedure. Thus it is worth comparing the reconstructed maps of permittivity obtained by first neglecting and then taking into account the interface in the inversion procedure. In Fig. 3(a), we neglect the interface in both the near- and far-field equations (4) and (6), respectively, that are solved at each iteration of the reconstruction algorithm. This is done by suppressing the susceptibility tensor of the interface, i.e., $\vec{\vec{\mathbf{S}}}^{\mathrm{d}}=\vec{\vec{\mathbf{S}}}=0$. We observe that the image is strongly deteriorated as compared with Fig. 2, and the two cubes are not resolved anymore. In Fig. 3(b), we neglect the susceptibility tensor of the interface in the near-field calculations only ($\vec{\vec{\mathbf{S}}}=0$). The reconstruction appears better than that in Fig. 3(a) but still less accurate than that obtained in Fig. 2. These numerical simulations show that accounting for the interface is mandatory, especially for the far-field calculations. This can be explained rather easily by comparing the field radiated by a dipole in free space with that radiated by a

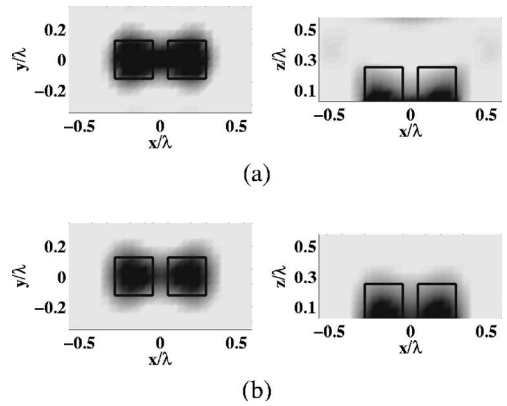

Fig. 3. Influence of the interface in the inverse scattering problem: (a) map of the relative permittivity when the interaction between the objects and the substrate is not taken into account ($\overleftrightarrow{\mathbf{S}}^{d}=\overleftrightarrow{\mathbf{S}}=0$), (b) map of the relative permittivity when the substrate is taken into account only in the far-field zone ($\overleftrightarrow{\mathbf{S}}=0$).

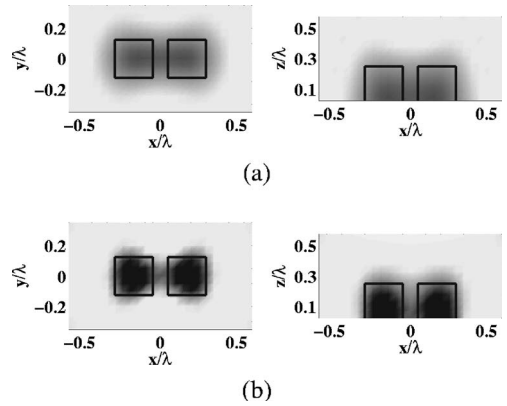

Fig. 4. Influence of the illuminations: (a) map of the relative permittivity with only propagative wave illuminations ($\theta^{inc}\in[-40,40]$ deg), (b) same as (a) but with evanescent wave illuminations ($\theta_l^{inc}\in[-80,-43]\cup[80,43]$ deg).

dipole placed in the vicinity of a plane interface. In the first case, the scattered far field radiated in the plane normal to the polarization of the dipole is constant whatever the direction of observation. In the second case, it tends to zero at grazing angles. Thus, accounting for the interface is most important for accurate modeling of the scattered far field. On the other hand, the error caused by neglecting the multiple scattering between the object and the interface in the evaluation of the field inside the object can be overlooked, in a first approximation, when both the diopter and the sample are dielectric with moderate permittivities. The advantage of this approximation is that solving the near-field equation (4) with the free-space susceptibility tensor yields an important time gain due to the convolution properties of the operator.[29]

B. Influence of Evanescent Illumination

We show in Figs. 4(a) and 4(b) the reconstructed maps of permittivity obtained when the incident angles belong to $[-40,40]$ and $[-80,43]\cup[43,80]$ deg, respectively. When the objects are illuminated by propagative waves only, it is impossible to distinguish the two cubes. On the contrary, if evanescent waves are used, one obtains an accurate reconstruction of the target, with sharp edges. Indeed, the transverse resolution is better the higher the spatial frequencies in the (x,y) plane of the incident plane waves.[9] When propagative waves are solely used, the horizontal components of the incident wave vectors are bounded by k_0, while they reach nk_0, where n is the refractive index of the prism, in the evanescent illumination configuration.

Figure 5 checks the influence of the position of the objects with respect to the interface in a complete illumination configuration $\theta_{inc}\in[-80,80]$ deg. The cube centers are placed 0.6λ above the prism. We observe that the reconstructed map of permittivity is close to that obtained when only propagative waves are used. Indeed, due to the exponential decay of the incident evanescent waves along the z axis, the far field scattered by the object when it is illuminated by an evanescent wave is negligible as compared with that scattered by the object when it is illuminated by a propagative wave. As a result, the weight of the evanescent illuminations in the cost functional is insufficient to elicit new information as compared with that given by propagative waves alone.

C. Influence of the Polarization

In Fig. 6, we plot the map of permittivity obtained under the complete illumination configuration but with s-polarized plane waves. The reconstructed image is close to that obtained with p-polarized waves (Fig. 2), although we observe that the edges are less accurately defined and the permittivity levels inside the cubes do not saturate in the same way. The p-polarized illuminations yield more accurate reconstructions than the s-polarized ones. This conclusion is not surprising inasmuch as the modulus of the incident evanescent waves at the surface of the prism is greater in p polarization than in s polarization. The weight of the evanescent illuminations in the cost functional being smaller in s polarization than in p polarization, the high-frequency features of the object are less defined.

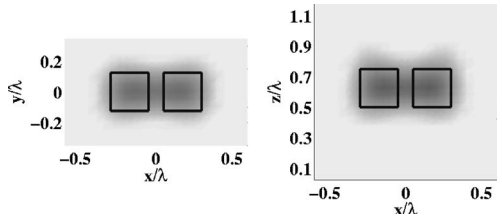

Fig. 5. Influence of the position of the sample with respect to the interface. This figure is the same as Fig. 2, except that the centers of the cubes are located at $z\approx 0.6\lambda$ from the interface.

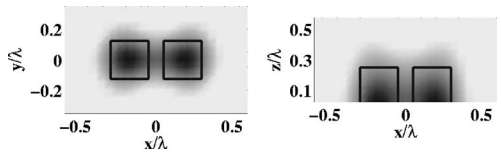

Fig. 6. Reconstruction of the permittivity using s-polarized wave illumination. The parameters are the same as those for Fig. 2.

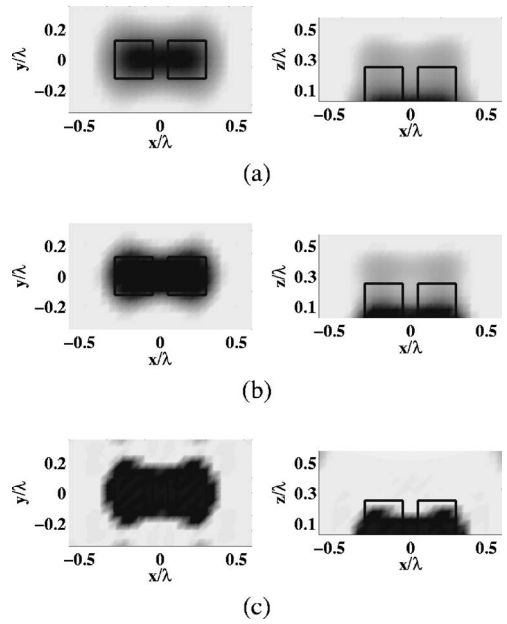

Fig. 7. Map of the relative permittivity in using the renormalized Born approximation: (a) with only propagative waves ($\theta^{\mathrm{inc}} \in [-40,40]$ deg), (b) with both propagative and evanescent waves ($\theta^{\mathrm{inc}} \in [-80,80]$ deg), (c) with only evanescent waves ($\theta_l^{\mathrm{inc}} \in [-80,-43] \cup [80,43]$ deg).

It is worth noting that one could enhance the high-frequency information by increasing artificially the weight of the far-field data stemming from the evanescent illuminations in the cost function. This remark holds also for the experiment depicted in Fig. 5. However, this technique can be applied only if the signal-to-noise ratio is high enough for the data obtained with evanescent illuminations to be meaningful.

D. Using the Renormalized Born Approximation

In this subsection, we present reconstructions obtained with a linear inversion technique based on the renormalized Born approximation. The latter consists in replacing the local near field given by Eq. (4) by the incident one. It is more accurate than the classical Born approximation, since it accounts for the static depolarization that occurs inside any dielectric, as shown in Appendix A. Under this approximation, one does not need to solve Eq. (4), and the computation time is greatly reduced. Note that, bearing in mind the remarks made in Subsection 4.A, the far-field equation (3) is calculated with the tensor of susceptibility that accounts for the interface. We observe in Fig. 7 that, whatever the incident illuminations (propagative, evanescent, or both), the reconstructed maps of permittivity do not permit the resolution of the two cubes, and the permittivity is overestimated close to the interface. This last point can be explained by noting that the local field inside a small sphere increases when the distance between the sphere and the interface decreases.[30] The renormalized Born approximation thus underestimates the field inside the objects, especially close to the interface. The inversion procedure compensates this error by overestimating the polarizability of the dipoles close to the interface.

E. Robustness with Respect to Noise

In this subsection, we analyze the robustness of our inversion scheme when an uncorrelated noise is added to the scattered field. This noise can be related to the detector background noise or to uncontrolled dust scattering. We corrupt each component of the scattered field as

$$\mathrm{Re}[\tilde{f}_{l;v}(\mathbf{r}_k)] = \mathrm{Re}[f_{l;v}(\mathbf{r}_k)] + uA_r\xi_{l;v}, \tag{16}$$

$$\mathrm{Im}[\tilde{f}_{l;v}(\mathbf{r}_k)] = \mathrm{Im}[f_{l;v}(\mathbf{r}_k)] + uA_i\eta_{l;v}, \tag{17}$$

where v stands for the component along x, y, or z. $\xi_{l;v}$ and $\eta_{l;v}$ are random numbers with uniform probability density in $[-1,1]$, and u is a real number smaller than unity that monitors the noise level. $A_r = \max[\mathrm{Re}(f_{l;v})] - \min[\mathrm{Re}(f_{l;v})]$, and $A_i = \max[\mathrm{Im}(f_{l;v})] - \min[\mathrm{Im}(f_{l;v})]$. Figure 8 shows the effect of the noise on the reconstructed maps of relative permittivity when the noise level u is equal to 20% for different configurations of illumination. Figure 8(a) shows the reconstruction when only evanescent waves are used, i.e., $\theta_l^{\mathrm{inc}} \in [-80,-43] \cup [80,43]$ deg. We observe that the reconstruction is relatively deteriorated by the presence of noise. This can be due to the fact that, in this configuration, the scattered far field obtained for the most evanescent incident waves, $\theta_{\mathrm{inc}} = 80$ deg, is totally blurred by the noise, whose level is related to the most important far-field intensity, i.e., that obtained for $\theta_{\mathrm{inc}} = 43$ deg. Thus, although these data do not reveal any information, their intensity becomes comparable with that obtained with moderate evanescent incident waves and they strongly perturb the reconstruction. In Fig. 8(b), we plot the map of permittivity obtained from noisy data in a complete configuration, containing both evanescent and propagative waves. Through the propagative waves, we have added low-spatial-frequency data that are less deteriorated by the noise and have suppressed several incident evanescent waves. We observe that the reconstruction becomes less sensitive to the noise and that, most important, the superresolution stemming from the use of evanescent illumination is still present. Hence it seems that using propagative together with evanescent wave illuminations permits one to increase the robustness to noise of

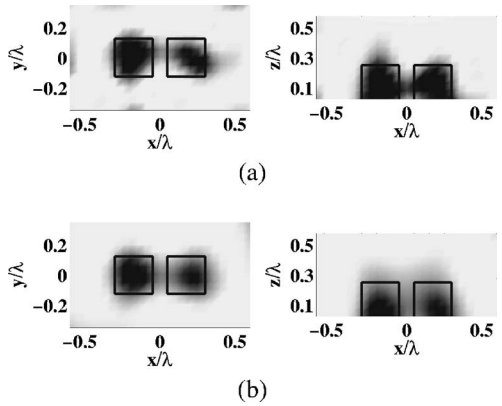

Fig. 8. Robustness of the inverse scattering algorithm with respect to uncorrelated noise: (a) map of the relative permittivity using only evanescent wave illuminations ($\theta_l^{\mathrm{inc}} \in [-80,-43] \cup [80,43]$ deg), (b) same as (a) but with both evanescent and propagative wave illuminations ($\theta^{\mathrm{inc}} \in [-80,80]$ deg).

the inversion procedure while retaining the superresolution.

5. CONCLUSION

We have simulated a realistic total internal reflection tomography (TIRT) experiment. We have proposed a full-vectorial nonlinear inversion scheme to retrieve the map of permittivity of the objects from the scattered far field. We have shown that it is possible to resolve two cubes of width $\lambda/4$ separated by $\lambda/10$ deposited on a prism made of glass ($\varepsilon=2.25$). We have investigated the power of resolution of our reconstructions with respect to the incident solid angle, the polarization, and the distance between the objects and the interface. We have presented a linear inversion method based on the renormalized Born approximation and pointed out that the presence of the interface restricts considerably the field of application of such a technique. Last, we have checked the influence of noise on the reconstructions. We have shown that adding propagative incident waves, together with evanescent ones, increases the robustness of our inversion procedure. To ameliorate the spatial resolution of the TIRT, it is necessary to generate evanescent waves with a large tangential wave vector. Unfortunately, in optics, the highest refractive index of the prism is about 2. Thus the resolution of the TIRT will be two times better than that of a standard tomography technique. To go further, one can modify the substrate so as to support high-frequency evanescent waves such as thin-film surface plasmons. Work in this direction is in progress.

APPENDIX A: BORN APPROXIMATION AND RENORMALIZED BORN APPROXIMATION

For the sake of simplicity, we explain the difference between the Born approximation and the renormalized Born approximation for an object in free space. Adding an interface does not change the explanation. The self-consistent electric field inside the object can be obtained from the following integral equation:

$$\mathbf{E}^{\mathrm{m}}(\mathbf{r}) = \mathbf{E}^{\mathrm{inc}}(\mathbf{r}) + \int_V \overleftrightarrow{\mathbf{T}}(\mathbf{r},\mathbf{r}')\chi(\mathbf{r}')\mathbf{E}^{\mathrm{m}}(\mathbf{r}')\mathrm{d}\mathbf{r}', \qquad \text{(A1)}$$

where $\mathbf{E}^{\mathrm{m}}(\mathbf{r})$ denotes the macroscopic field inside the object and $\chi(\mathbf{r}')=[\varepsilon(\mathbf{r}')-1]/(4\pi)$ is the linear susceptibility of the object. $\overleftrightarrow{\mathbf{T}}$ is the free-space susceptibility tensor,[31] given by

$$\overleftrightarrow{\mathbf{T}}(\mathbf{r},\mathbf{r}') = \exp(ik_0R)\left[\left(3\frac{\mathbf{R}\otimes\mathbf{R}}{R^2}-\overleftrightarrow{\mathbf{I}}\right)\left(\frac{1}{R^3}-\frac{ik_0}{R^2}\right) + \left(\overleftrightarrow{\mathbf{I}}-\frac{\mathbf{R}\otimes\mathbf{R}}{R^2}\right)\frac{k_0^2}{R}\right] - \frac{4\pi}{3}\overleftrightarrow{\mathbf{I}}\delta(\mathbf{R}), \qquad \text{(A2)}$$

where $\mathbf{R}=\mathbf{r}-\mathbf{r}'$, $R=|\mathbf{R}|$, k_0 is the free-space wave number, and $\overleftrightarrow{\mathbf{I}}$ is the unit tensor. To solve Eq. (A1), we discretize the object into N subunits, arranged on a cubic lattice. The size d of the elementary cell is small enough that the macroscopic field can be considered constant over it (typically, the cell side is one tenth of the wavelength in the object). The discretized Eq. (A1) reads as

$$\mathbf{E}^{\mathrm{m}}(\mathbf{r}_i) = \mathbf{E}^{\mathrm{inc}}(\mathbf{r}_i) + \sum_{j=1,j\neq i}^{N} \overleftrightarrow{\mathbf{T}}(\mathbf{r}_i,\mathbf{r}_j)\chi(\mathbf{r}_j)d^3\mathbf{E}^{\mathrm{m}}(\mathbf{r}_j) - \frac{\varepsilon(\mathbf{r}_i)-1}{3}\mathbf{E}^{\mathrm{m}}(\mathbf{r}_i). \qquad \text{(A3)}$$

If we factorize the terms corresponding to index i, we get an equation for the local field,

$$\mathbf{E}(\mathbf{r}_i) = \mathbf{E}^{\mathrm{inc}}(\mathbf{r}_i) + \sum_{j=1,j\neq i}^{N} \overleftrightarrow{\mathbf{T}}(\mathbf{r}_i,\mathbf{r}_j)\alpha(\mathbf{r}_j)\mathbf{E}(\mathbf{r}_j), \qquad \text{(A4)}$$

where the macroscopic field and the local field are linked by the relation

$$\frac{\varepsilon+2}{3}\mathbf{E}^{\mathrm{m}}(\mathbf{r}_i) = \mathbf{E}(\mathbf{r}_i). \qquad \text{(A5)}$$

Equation (A4) is the usual form of the CDM introduced by Purcell and Pennypacker.[13]

The so-called Born approximation consists in the hypothesis that the macroscopic field inside the object is close to the incident field, i.e., Eq. (A1) is reduced to $\mathbf{E}^{\mathrm{m}}(\mathbf{r}_i)=\mathbf{E}^{\mathrm{inc}}(\mathbf{r}_i)$. The renormalized Born approximation amounts to assimilating the local field inside the object to the incident field; hence Eq. (A4) is reduced to $\mathbf{E}(\mathbf{r}_i) \approx \mathbf{E}^{\mathrm{inc}}(\mathbf{r}_i)$. In this case, the relation between the macroscopic field and the incident field reads as

$$\mathbf{E}^{\mathrm{m}}(\mathbf{r}_i) \approx \frac{3}{\varepsilon+2}\mathbf{E}^{\mathrm{inc}}(\mathbf{r}_i). \qquad \text{(A6)}$$

This approximation is thus different from the classical Born approximation. It is more accurate than the latter, especially when the dielectric contrast between the object and the surrounding medium is high.[32]

APPENDIX B: EXPRESSION OF THE SURFACE FIELD SUSCEPTIBILITY

In this appendix, we express the elements of the tensor of the surface field susceptibility $\overleftrightarrow{\mathbf{S}}$. In general, the tensor in the presence of an interface normal to the z axis is given, in Cartesian coordinates, under the Weyl development.[18] It requires the numerical calculation of a two-dimensional Fourier transform over the conjugate variables of x and y. Here we propose an alternative expression of the surface field susceptibility, in cylindrical coordinates, that necessitates a single numerical integration.

The dyadic tensor has nine components, but the symmetry of the surface suggests some relations between the elements of the tensor. Hence only four integrals are needed to derive all the elements. Let the angle φ be defined by

$$a=[(x-x_0)^2+(y-y_0)^2]^{1/2},$$

$$\sin\varphi=(x-x_0)/a,$$

$$\cos\varphi=(y-y_0)/a, \tag{B1}$$

where (x,y,z) is the position of the observation point and (x_0,y_0,z_0) the location of the dipole. Let us also define the Fresnel reflection coefficients Δ_s and Δ_p for s- and p-polarized plane or evanescent waves:

$$\Delta_p=\frac{w_1-\varepsilon_s w_0}{w_1+\varepsilon_s w_0},\qquad \Delta_s=\frac{w_1-w_0}{w_1+w_0}, \tag{B2}$$

with $w_1^2=\varepsilon_s k_0^2-u^2$ and $w_0^2=k_0^2-u^2$. u is the modulus of the wave vector parallel to the surface. $\overleftrightarrow{\mathbf{S}}$ can be written as[33]

$$\overleftrightarrow{\mathbf{S}}(\mathbf{r},\mathbf{r}_0)=\begin{bmatrix} I_1+\cos(2\varphi)I_2 & -\sin(2\varphi)I_2 & \sin\varphi I_3 \\ -\sin(2\varphi)I_2 & I_1-\cos(2\varphi)I_2 & \cos\varphi I_3 \\ -\sin\varphi I_3 & -\cos\varphi I_3 & I_4 \end{bmatrix}, \tag{B3}$$

with

$$I_1=\frac{i}{2}\left(-\int_0^{k_0}+\int_0^{i\infty}\right)\mathrm{d}w_0 J_0(au)\exp[iw_0(z+z_0)]\times(k_0^2\Delta_s-w_0^2\Delta_p), \tag{B4}$$

$$I_2=\frac{i}{2}\left(-\int_0^{k_0}+\int_0^{i\infty}\right)\mathrm{d}w_0 J_0(au)\exp[iw_0(z+z_0)]\times(-k_0^2\Delta_s-w_0^2\Delta_p), \tag{B5}$$

$$I_3=\left(-\int_0^{k_0}+\int_0^{i\infty}\right)\mathrm{d}w_0 J_1(au)\exp[iw_0(z+z_0)]\Delta_p w_0 u, \tag{B6}$$

$$I_4=i\left(-\int_0^{k_0}+\int_0^{i\infty}\right)\mathrm{d}w_0 J_0(au)\exp[iw_0(z+z_0)]\Delta_p u^2. \tag{B7}$$

The functions J_0, J_1, and J_2 are Bessel functions of the first kind and are zero, first, and second order, respectively. Equations (B4)–(B7) correspond to the sum of two integrals: One is evaluated over the propagative waves, and the second over the evanescent waves. When $a=0$, $\overleftrightarrow{\mathbf{S}}$ becomes diagonal.

APPENDIX C: EXPRESSION IN THE FAR-FIELD ZONE OF THE SURFACE FIELD SUSCEPTIBILITY

When the observation point is in the far field, one can use the method of stationary phase[34] for computing the surface field susceptibility tensor $\overleftrightarrow{\mathbf{S}}^{\mathrm{d}}$:

$$\overleftrightarrow{\mathbf{S}}^{\mathrm{d}}(\mathbf{r},\mathbf{r}_0)=\frac{k_0^2}{r}\exp\{ik_0[x(x-x_0)+y(y-y_0)+z(z+z_0)]/r\}\times\begin{bmatrix} \left(\frac{xz}{r\rho}\right)^2\Delta_p'-\frac{y^2}{\rho^2}\Delta_s' & \frac{xy}{\rho^2}\left(\frac{z^2}{r^2}\Delta_p'+\Delta_s'\right) & \frac{xz}{r^2}\Delta_p' \\ \frac{xy}{\rho^2}\left(\frac{z^2}{r^2}\Delta_p'+\Delta_s'\right) & \left(\frac{yz}{r\rho}\right)^2\Delta_p'-\frac{x^2}{\rho^2}\Delta_s' & \frac{yz}{r^2}\Delta_p' \\ -\frac{xz}{r^2}\Delta_p' & -\frac{yz}{r^2}\Delta_p' & -\frac{\rho^2}{r^2}\Delta_p' \end{bmatrix}, \tag{C1}$$

with $r=(x^2+y^2+z^2)^{1/2}$ and $\rho=(x^2+y^2)^{1/2}$. The Fresnel reflection coefficients are given by

$$\Delta_p'=\frac{(\varepsilon_s r^2-\rho^2)^{1/2}-\varepsilon_s z}{(\varepsilon_s r^2-\rho^2)^{1/2}+\varepsilon_s z},\quad \Delta_s'=\frac{(\varepsilon_s r^2-\rho^2)^{1/2}-z}{(\varepsilon_s r^2-\rho^2)^{1/2}+z}. \tag{C2}$$

If $x=y=0$, then

$$\overleftrightarrow{\mathbf{S}}^{\mathrm{d}}(z,z_0)=\frac{k_0^2}{z}\exp[ik_0(z+z_0)]\begin{bmatrix}\Delta_p' & 0 & 0\\ 0 & \Delta_p' & 0\\ 0 & 0 & 0\end{bmatrix}. \tag{C3}$$

The analytical form of $\overleftrightarrow{\mathbf{S}}^{\mathrm{d}}$ permits a quick computation of the matrix $\bar{\bar{\mathbf{B}}}$.

APPENDIX D: BACKPROPAGATION PROCEDURE TO GENERATE AN INITIAL GUESS TO THE ITERATIVE INVERSE SCATTERING ALGORITHM

We present here the derivation of an initial guess that is used to start the iterative scheme described in Section 3. First, we determine, for each illumination l, an estimation of the dipole distribution $\mathbf{p}_l^{\mathrm{init}}$ lying in the investigating domain Ω by backpropagating the measured fields $\mathbf{f}_l$ into Ω:

$$\mathbf{p}_l^{\mathrm{init}}=\gamma_l\bar{\bar{\mathbf{B}}}^{\dagger}\mathbf{f}_l, \tag{D1}$$

where $\bar{\bar{\mathbf{B}}}^{\dagger}$ denotes the transpose complex conjugate matrix of the matrix $\bar{\bar{\mathbf{B}}}$. The scalar weight γ_l is determined by minimizing the cost function $\mathcal{M}(\gamma_l)$ describing the discrepancy between the data $\mathbf{f}_l$ and those that would be obtained with $\mathbf{p}_l^{\mathrm{init}}$:

$$\mathcal{M}(\gamma_l)=\|\mathbf{f}_l-\bar{\bar{\mathbf{B}}}\mathbf{p}_l^{\mathrm{init}}\|_{\Gamma}^2=\|\mathbf{f}_l-\gamma_l\bar{\bar{\mathbf{B}}}\bar{\bar{\mathbf{B}}}^{\dagger}\mathbf{f}_l\|_{\Gamma}^2. \tag{D2}$$

Writing down the necessary condition $\partial\mathcal{M}/\partial\gamma_l=0$ for $\mathcal{M}$ to be a minimum leads to an analytical expression of γ_l:

$$\gamma_l=\frac{\langle\bar{\bar{\mathbf{B}}}\bar{\bar{\mathbf{B}}}^{\dagger}\mathbf{f}_l|\mathbf{f}_l\rangle_{\Gamma}}{\|\bar{\bar{\mathbf{B}}}\bar{\bar{\mathbf{B}}}^{\dagger}\mathbf{f}_l\|_{\Gamma}^2}. \tag{D3}$$

Once the estimation of the dipoles is determined, an estimation of the total field $\mathbf{E}_l^{\mathrm{init}}$ in the investigating domain Ω can be derived either by assuming the Born approximation or by applying Eq. (4):

$$\mathbf{E}_l^{\text{init}} = \mathbf{E}_l^{\text{inc}} + \bar{\bar{\mathbf{A}}}\mathbf{p}_l^{\text{init}}. \tag{D4}$$

Finally, the initial guess for the polarizability distribution α^{init} at a position $\mathbf{r}$ inside Ω is deduced from $\mathbf{p}_l^{\text{init}}$ and $\mathbf{E}_l^{\text{init}}$ as follows:

$$\alpha^{\text{init}}(\mathbf{r}) = \text{Re}\left[\frac{\sum_{l=1}^{L} \mathbf{p}_l^{\text{init}}(\mathbf{r}) \cdot \mathbf{E}_l^{\text{init}^*}(\mathbf{r})}{\sum_{l=1}^{L} \|\mathbf{E}_l^{\text{init}}(\mathbf{r})\|^2}\right]. \tag{D5}$$

K. Belkebir's e-mail address is kamal.belkebir @fresnel.fr.

REFERENCES

1. M. Gustafsson, "Surpassing the lateral resolution limit by a factor of two using structured illumination microscopy," J. Microsc. **198**, 82–87 (2000).
2. N. Destouches, C. A. Guérin, M. Lequime, and H. Giovannini, "Determination of the phase of the diffracted field in the optical domain. Application to the reconstruction of surface profiles," Opt. Commun. **198**, 233–239 (2001).
3. V. Lauer, "New approach to optical diffraction tomography yielding a vector equation of diffraction tomography and a novel tomographic microscope," J. Microsc. **205**, 165–176 (2002).
4. T. Wedberg and J. Stammes, "Experimental examination of the quantitative imaging properties of optical diffraction tomography," J. Opt. Soc. Am. A **12**, 493–500 (1995).
5. D. Fischer, "Subwavelength depth resolution in near-field microscopy," Opt. Lett. **25**, 1529–1531 (2000).
6. P. So, H. Kwon, and C. Dong, "Resolution enhancement in standing-wave total-internal reflection microscopy: a point spread function engineering approach," J. Opt. Soc. Am. A **18**, 2833–2845 (2001).
7. F. de Fornel, *Evanescent Waves*, Vol. 73 of Springer Series in Optical Sciences (Springer Verlag, 2001).
8. G. Cragg and P. So, "Standing wave total-internal reflection microscopy," Opt. Lett. **25**, 46–48 (2000).
9. P. S. Carney and J. C. Schotland, "Three-dimensional total-internal reflection microscopy," Opt. Lett. **26**, 1072–1074 (2001).
10. E. Wolf, "Three-dimensional structure determination of semi-transparent objects from holographic data," Opt. Commun. **1**, 153–156 (1969).
11. K. Belkebir and A. Sentenac, "High resolution optical diffraction microscopy," J. Opt. Soc. Am. A **20**, 1223–1229 (2003).
12. P. C. Chaumet, K. Belkebir, and A. Sentenac, "Superresolution of three-dimensional optical imaging by use of evanescent waves," Opt. Lett. **29**, 2740–2742 (2004).
13. E. M. Purcell and C. R. Pennypacker, "Scattering and absorption of light by nonspherical dielectric grains," Astrophys. J. **186**, 705–714 (1973).
14. P. C. Chaumet and M. Nieto-Vesperinas, "Time-averaged total force on a dipolar sphere in an electromagnetic field," Opt. Lett. **25**, 1065–1067 (2000).
15. A. Lakhtakia, "Strong and weak forms of the method of moments and the coupled dipole method for scattering of time-harmonic electromagnetics fields," Int. J. Mod. Phys. C **3**, 583–603 (1992).
16. P. C. Chaumet, A. Sentenac, and A. Rahmani, "Coupled dipole method for scatterers with large permittivity," Phys. Rev. E **70**, 036606 (2004).
17. S. Kawata, O. Nakamura, and S. Minami, "Optical microscope tomography. I. Support constraint," J. Opt. Soc. Am. A **4**, 292–297 (1987).
18. P. S. Carney and J. C. Schotland, "Theory of total-internal-reflection tomography," J. Opt. Soc. Am. A **20**, 542–547 (2003).
19. A. G. Tijhuis, K. Belkebir, A. C. S. Litman, and B. P. de Hon, "Theoretical and computational aspects of 2-D inverse profiling," IEEE Trans. Geosci. Remote Sens. **39**, 1316–1330 (2001).
20. R. E. Kleinman and P. M. van den Berg, "A modified gradient method for two-dimensional problems in tomography," J. Comput. Appl. Math. **42**, 17–35 (1992).
21. K. Belkebir and A. G. Tijhuis, "Modified^2 gradient method and modified Born method for solving a two-dimensional inverse scattering problem," Inverse Probl. **17**, 1671–1688 (2001).
22. P. C. Chaumet, K. Belkebir, and A. Sentenac, "Three-dimensional subwavelength optical imaging using the coupled dipole method," Phys. Rev. B **69**, 245405 (2004).
23. A. Abubakar, P. M. van den Berg, and B. J. Kooij, "A conjugate gradient contrast source technique for 3D profile inversion," IEICE Trans. Electron. **E83-C**, 1864–1874 (2000).
24. A. Abubakar and P. M. van den Berg, "The contrast source inversion method for location and shape reconstructions," Inverse Probl. **18**, 495–510 (2002).
25. W. H. Press, B. P. Flannery, S. A. Teukolski, and W. T. Vetterling, *Numerical Recipes: The Art of Scientific Computing* (Cambridge U. Press, 1986).
26. K. Belkebir, S. Bonnard, F. Pezin, P. Sabouroux, and M. Saillard, "Validation of 2D inverse scattering algorithms from multi-frequency experimental data," J. Electromagn. Waves Appl. **14**, 1637–1667 (2000).
27. K. Belkebir, R. E. Kleinman, and C. Pichot, "Microwave imaging—location and shape reconstruction from multifrequency scattering data," IEEE Trans. Microwave Theory Tech. **45**, 469–476 (1997).
28. R. E. Kleinman and P. M. van den Berg, "Two-dimensional location and shape reconstruction," Radio Sci. **29**, 1157–1169 (1994).
29. J. J. Goodman, B. T. Draine, and P. J. Flatau, "Application of fast-Fourier-transform techniques to the discrete-dipole approximation," Opt. Lett. **16**, 1198–1200 (1991).
30. F. Pincemin, A. Sentenac, and J.-J. Greffet, "Near-field scattered by a dielectric rod below a metallic surface," J. Opt. Soc. Am. A **11**, 1117–1127 (1994).
31. J. D. Jackson, *Classical Electrodynamics*, 2nd ed. (Wiley, 1975).
32. T. M. Habashy, R. W. Groom, and B. R. Spies, "Beyond the Born and Rytov approximations—a nonlinear approach to electromagnetic scattering," J. Geophys. Res. [Solid Earth] **98**, 1759–1775 (1993).
33. A. Rahmani, P. C. Chaumet, F. de Fornel, and C. Girard, "Field propagator of a dressed junction: fluorescence lifetime calculations in a confined geometry," Phys. Rev. A **56**, 3245–3254 (1997).
34. M. Born and E. Wolf, *Principles of Optics* (Pergamon, 1959).